

# CoinFT: A Coin-Sized, Capacitive 6-Axis Force Torque Sensor for Robotic Applications

Hojung Choi<sup>\*1</sup>, Jun En Low<sup>\*1</sup>, Tae Myung Huh<sup>2</sup>, Seongheon Hong<sup>1</sup>, Gabriela A. Uribe<sup>1</sup>, Kenneth A. W. Hoffmann<sup>1</sup>, Julia Di<sup>1</sup>, Tony G. Chen<sup>1</sup>, Andrew A. Stanley<sup>3</sup>, and Mark R. Cutkosky<sup>1</sup>

**Abstract**—We introduce CoinFT, a capacitive 6-axis force/torque (F/T) sensor that is compact, light, low-cost, and robust with an average root-mean-squared error of 0.16 N for force and 1.08 mNm for moment when the input ranges from 0~14 N and 0~5 N in normal and shear directions, respectively. CoinFT is a stack of two rigid PCBs with comb-shaped electrodes connected by an array of silicone rubber pillars. The microcontroller interrogates the electrodes in different subsets in order to enhance sensitivity for measuring 6-axis F/T. The combination of features of CoinFT enables various contact-rich robot interactions across different embodiment domains including drones, robot end-effectors, and wearable haptic devices. We demonstrate the utility of CoinFT through two representative applications: a multi-axial contact-probing experiment in which a CoinFT mounted beneath a hemispherical fingertip measures 6-axes of force and torque representative of manipulation scenarios, and an attitude-based force-control task on a drone. The design, fabrication, and firmware of CoinFT are open-sourced at <https://coin-ft.github.io/>.

**Index Terms**—Force and Tactile Sensing, Sensor Design, Force Control, Perception for Grasping and Manipulation

## I. INTRODUCTION

**P**RECISE force and torque measurement is vital for robots to perform contact-rich tasks safely and effectively. Tasks such as table wiping [1], assembly [2], or palpating soft tissue [3] require the application of force and torque within a specific range—sufficient to complete the task but not excessive, as to cause damage or waste energy. Depending on the application and interaction type, robots performing contact-rich tasks come in various forms, including robotic arms [4], grippers [5], drones [6], and wearable devices [7]. Therefore, it is highly desirable to develop a compact and low cost solution that can serve a wide variety of applications.

Extensive research has been dedicated to developing 6-axis force/torque (F/T) sensors using various transduction methods [8]. Commercially available sensors also exist, such as the Gamma™ (ATI Industries), and 6-axis F/T sensors from MinebeaMitsumi™ or ReSense™. However, these sensors are challenging to adopt across different robotic platforms, particularly those requiring both robustness and small, slim form factors. For example, while commercial sensors can be compact and lightweight, they are often too fragile to reliably withstand impacts from drone crashes or incidental contact on an end-effector. Their thickness also adds unnecessary bulk to haptic devices, making them cumbersome. Additionally,

the cost of these sensors can be prohibitive, especially when attempting to sensorize multiple fingers of anthropomorphic robot hands such as the Leap hand [9]. Other sensors that are robust and more affordable tend to be bulky [10], limiting their applicability in compact platforms.

In this paper, we introduce CoinFT, a capacitive 6-axis F/T sensor the size of a US quarter dollar, weighing 2 g (Fig. 1 (a)), with a material cost of less than \$ 11 (Table II). CoinFT combines the aforementioned desirable features, unlocking various contact-rich robot interactions in unstructured environments.

We validate CoinFT’s multi-axis sensing capability through a contact-probing experiment, where a 7-DoF robotic arm applies controlled 6-axis F/T on a fingertip-mounted CoinFT. This setup demonstrates CoinFT’s suitability for fine-grained manipulation scenarios while maintaining a compact fingertip-scale form factor.

Another promising application for CoinFT is on drones performing forceful interactions with the environment. Drones have previously executed contact-rich tasks without force feedback [11] in controlled scenarios or through careful human teleoperation [6]. While force sensors have been demonstrated in such tasks, their size, weight, and fragility make them unsuitable for unstructured, environments [12]. CoinFT’s design addresses these challenges, making it a viable solution for drones operating in environments where large impulses from contact or crashes are common. Its lightweight nature minimally impacts drone operation time, and its compact size facilitates easy integration into even small drones. In this work, we demonstrate the use of CoinFT on a drone for contact modulation through PID force control and the deployment of objects onto environmental surfaces by applying a controlled range of force.

The contributions of this paper are as follows:

- The design, fabrication, and comprehensive characterization of CoinFT.
- Experimental validation of CoinFT on multiple robotic platforms, including a contact-probing experiment demonstrating accurate multi-axis sensing at the fingertip scale and a drone performing contact-force modulation.
- Open-sourcing the design, fabrication, and firmware of CoinFT.

## II. RELATED WORK

### A. Multi-axial Force Torque Sensors

Given the role of forces in contact-rich tasks, significant research has focused on developing multi-axial F/T sensors

<sup>1</sup>Stanford University, CA, USA.

<sup>2</sup>University of California Santa Cruz, CA, USA.

<sup>3</sup>Reality Labs Research, Meta Platforms Inc, WA, USA.

using diverse transduction methods, including piezoresistive, capacitive, optical, magnetic, and pneumatic techniques [8]. Among these, piezoresistive approaches have been the most extensively explored, typically involving the attachment of multiple strain gauges to precisely machined structures, commonly designed as cross-beam or parallel structures [8]. Piezoresistive sensing offers precise measurement capabilities with a high signal-to-noise ratio (SNR), facilitated by strain gauges and circuitry optimized for SNR amplification [13]. The availability of compact electronics and advanced machining techniques has also enabled the fabrication of compact sensors, which is why commercially available 6-axis F/T sensors predominantly utilize piezoresistive technology (e.g. MinebeaMitsumi™ and ReSense™). However, these sensors are often fragile and susceptible to impact, which can result in plastic deformation or even failure of the sensing medium [14].

Capacitive sensing is another widely adopted approach for designing 6-axis F/T sensors, valued for its potential to achieve a compact form factor while maintaining high sensitivity [8]. Compared to piezoresistive sensors, capacitive sensors can be relatively simpler to fabricate. Multiaxial F/T sensing via capacitive methods is typically achieved in one of two ways. The first uses a single layer of sensing electrodes integrated with specially designed structures that deform to produce distinct signal patterns upon loading [16], [18], [19].

However, such single-layer designs often require complex fabrication processes and specialized equipment for custom machining or microstructuring, which limits scalability. The second approach employs multi-layer electrode stacks, where each layer responds to specific subsets of forces and torques to generate distinguishable signal patterns [20]. While effective, these architectures introduce additional fabrication complexity and can be bulkier, making them less suitable for applications that require compactness. The CoinFT design draws inspiration from multi-layer capacitive architectures but achieves comparable multi-axis capability using a single pair of sensing electrodes through an efficient mode-switching and sampling strategy, as discussed in Section III-A.

Optical sensing methods have been employed in the design of multi-axis F/T sensors by controlling the scattering or reflection of light within the system [21]. These methods can be broadly categorized into light intensity sensing [22], employing Fiber Bragg Grating (FBG) optical fibers [23], and vision-based techniques. In traditional optical methods, variations in reflected light intensity at multiple locations are converted into measurements of force and torque [22]. FBG-based sensing leverages FBG fibers embedded in areas of higher strain within the sensor body, functioning similarly to strain gauges to precisely measure deformation [23]. Vision-based tactile sensing involves using a compact camera to observe the deformation of a silicone rubber medium, often a

TABLE I  
COMPARISON OF REPRESENTATIVE LOWER-COST 6-AXIS FORCE/TORQUE SENSORS FOR ROBOTIC APPLICATIONS

Sensor	Transduction	Size [mm]	Mass	Sensing range	Accuracy (R <sup>2</sup> or % error)	Bandwidth	Cost	Robustness
MinebeaMitsumi™ 6-axis F/T sensor	Piezoresistive	$\phi 9.6 \times t 9$	3 g	F: 40 N T: 400 mN·m	Full-scale error: $\pm 5\%$	1 kHz	\$1200+	No
Guggenheim et al. [10]	Barometric (MEMS)	75 × 75 × 30	N/A	$F_{x,y}$ : 5 N $F_z$ : 12 N T: 3000 mN·m	$F_x$ : 0.937 $F_y$ : 0.909 $F_z$ : 0.998 $M_x$ : 0.984 $M_y$ : 0.984 $M_z$ : 0.991	50 Hz	\$20	Yes
Ouyang et al. [15]	Vision (Camera)	36 × 31 × 51	N/A	$F_{x,y}$ : 2 N $F_z$ : 1 N $T_{x,y}$ : 100 mN·m $T_z$ : 4 mN·m	$F_x$ : 0.991 $F_y$ : 0.996 $F_z$ : 0.875 $M_x$ : 0.997 $M_y$ : 0.998 $M_z$ : 0.902	25 Hz (sampling)	\$40	Yes
Kim et al. [16]	Capacitive	14 × 17 × 6.5	2.6 g	F: 30 N M: 300 mN·m	Full-scale error: Fx: 0.92% Fy: 0.83% Fz: 1.57% Mx: 2.8% My: 2.1% Mz: 3.4%	200 Hz (sampling) <5 Hz (mech. estimated)	N/A	N/A
El-Azizi et al. [17]	Optical	$\phi 27 \times t 20$	16.4 g	F: 10 N M: 200 mN·m	$F_x$ : 0.990 $F_y$ : 0.993 $F_z$ : 0.560 $M_x$ : 0.995 $M_y$ : 0.991 $M_z$ : 0.923	2.5 kHz (sampling)	\$100	Yes
CoinFT (this work)	Capacitive	$\phi 20 \times t 2$	2 g	$F_{x,y}$ : 5 N $F_z$ : 15 N $T_{x,y}$ : 100 mN·m $T_z$ : 80 mN·m	$F_x$ : 0.983 $F_y$ : 0.983 $F_z$ : 0.998 $M_x$ : 0.988 $M_y$ : 0.987 $M_z$ : 0.989	360 Hz (sampling) 100 Hz (mech.)	\$11	Yes

robot fingertip, upon contact [24]–[26]. A recently popularized approach for force and torque sensing involves monitoring the deformation of specially patterned silicone rubber fingertips and employing data-driven models to infer the applied force and torque [25], [27], [28]. Another method involves tracking the movement of a visual cue with a camera to deduce the load [29], [30]. Alternatively, gel deformation patterns can be remotely observed through an optical fiber, enabling the decoupling of the silicone gel from the sensing camera [31].

Other, less explored approaches in the design of multi-axial F/T sensors include piezoelectric [32], magnetic [33], [34], and pneumatic methods [10]. While piezoelectric effects have been utilized in these sensors, their susceptibility to charge leakage makes them less ideal for measuring static loads. Magnetic sensing techniques, which involve strategically positioning magnets and Hall effect sensors to detect forces and torques across six axes, have also been explored [33]. However, magnetic sensing is inherently vulnerable to external noise sources, such as the Earth’s magnetic field or nearby ferromagnetic objects. Additionally, similar design principles have been applied in pressure sensors, where differential patterns are created using an array of barometers [10].

Among the various 6-axis F/T sensors reported in prior work, Table I compares representative designs that emphasize compact form factors and relatively low cost, including both research prototypes and commercial devices. CoinFT combines several desirable attributes such as compact and low-profile design, reasonable accuracy across all six axes, mechanical robustness, and affordability, within a single platform. This balance of performance and practicality enables a wide range of robotic applications, including wearable haptic interfaces [7], [35], dexterous manipulation [36], and drone-based interaction tasks, as demonstrated in Section IV-B.

### B. Contact Based Interaction of Drones

Significant research has focused on enabling drones to avoid contact [37], and more recently, efforts have shifted toward allowing drones to interact with their environment through controlled and sustained contact, such as in perching [38] or performing tasks that require contact modulation [39]. Perching, in particular, has garnered attention for its ability to allow drones to remain in an environment without expending energy to stay aloft, thereby significantly increasing their operational time. To facilitate perching on horizontal [40] and vertical surfaces [41], bioinspired grippers [42] and control strategies [11] have been developed. While these approaches show promise for perching, they typically lack contact sensing, which limits the ability to assess perch stability or react to failures in real-time.

Recent research has explored the use of force-controlled contact with the environment through the integration of load cells [43]. These studies have investigated various applications, such as maintaining a consistent contact force while changing position using hybrid position-force controllers [44], analyzing surface textures by combining load cells with vision-based tactile sensors [12], and attaching objects to surfaces with custom-designed mechanisms [43]. However, the load cells

used in these studies, typically commercial 6-axis F/T sensors, present challenges for real-world integration due to their high cost, fragility, and bulky readout electronics. In contrast, CoinFT, with its lightweight, compact design, robustness, and affordability, is ideally suited for drone applications.

## III. COINFT

### A. CoinFT Design

CoinFT is a capacitive 6-axis force/torque sensor. Its circular sensing area is 20 mm in diameter and approximately 2 mm in thickness (Fig. 1 (c)), having a comparable form-factor to a quarter-dollar coin in the United States currency (Fig. 1 (a)). With a total weight of 2 g, it consists of two 0.8 mm thick rigid PCBs (Printed Circuit Boards) connected by an array of 127  $\mu\text{m}$  tall cylindrical pillars cast from silicone rubber (TAP<sup>®</sup> Silicone RTV Mold-Making System). Solid pillars were selected as they provide favorable sensitivity in both normal and shear directions without compromising bandwidth [45], [46]. Silicone rubber was chosen as the pillar material because alternatives such as polyurethane exhibit higher viscoelastic damping and reduced bandwidth [47]–[50]. The radial density of pillars increases towards the edge of the PCB for improved strength against delamination. We employ a dense array of microns-wide pillars, despite the added challenges in fabrication, to retain sensitivity. Wider structures will increase effective stiffness of the pillar layer, which will be discussed in detail in Section III-D.

Each rigid PCB is multilayered, with four quadrants of a pair of comb-shaped electrodes on one side and a plane electrode for passive shielding on the other side (Fig. 1 (b), (c)). The upper sensing layer has eight physical electrodes while the lower sensing layer houses two physical electrodes (Fig. 1 (b)). It is by leveraging this design with the unique capabilities of the microcontroller (Cypress, PSoC<sup>™</sup> 4100S) on CoinFT, that a pair of PCBs becomes sensitive to six axes of force and torque, which will be discussed in detail in Section III-B. The top shield layer made of a 127  $\mu\text{m}$  thick fPCB (flexible Printed Circuit Board) is then added to provide additional passive shielding, as the via holes in the upper sensing layer can introduce noise from stray capacitance in the environment (Fig. 1 (b), (c)). Each PCB layer has an alignment tab on its sides, which are later removed during the final stages of fabrication.

An electronics tab (10 mm  $\times$  11 mm) attached to the side of the circular sensing area houses the electronics necessary for capacitance sensing (Fig. 1 (b), (c)). A microcontroller with external capacitors measures and converts capacitance to digital counts using its native capacitance-to-digital conversion (CDC) module at 360 Hz. Signals can be acquired by other devices through direct serial communication or USB ports through a serial to USB converter, such as a PSoC<sup>™</sup> KitProg2, with a latency of 2 ms on average.

### B. Working Principle

CoinFT measures 6-axis force and torque by observing the changes in capacitance signal patterns between the upper

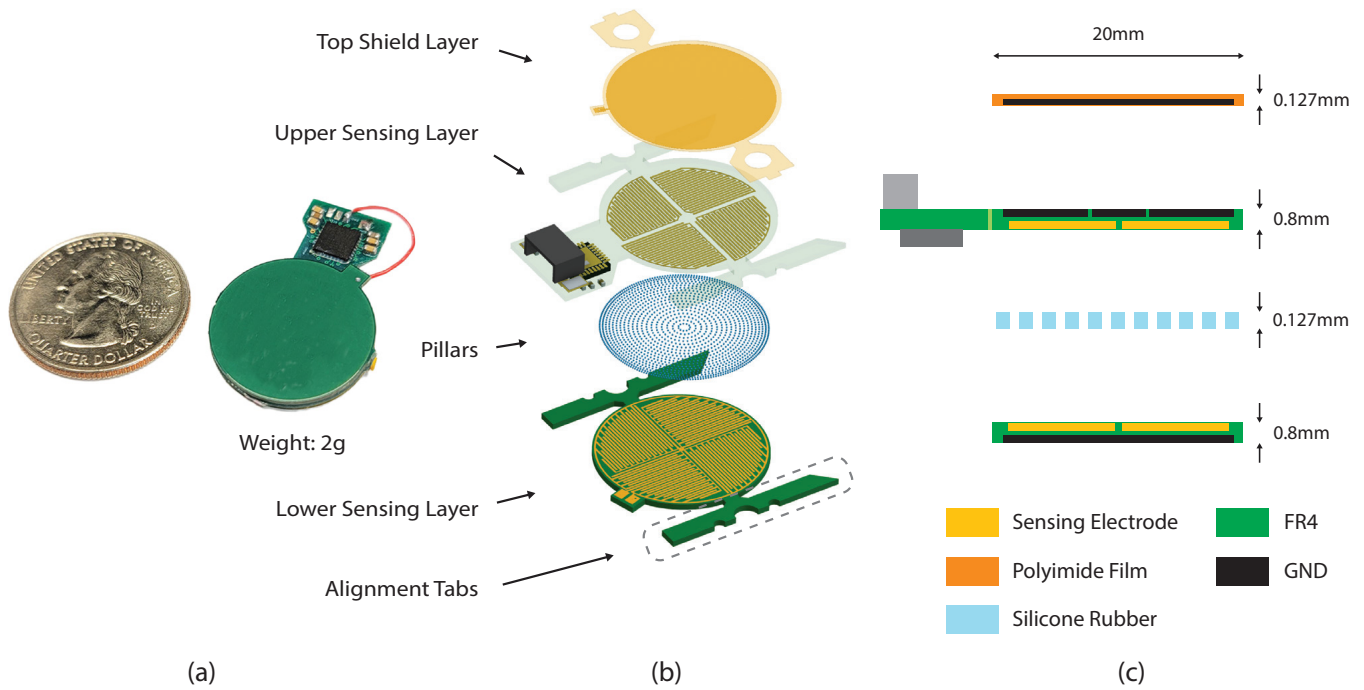


Fig. 1. (a) CoinFT is approximately the size of a U.S. quarter-dollar coin. (b) Exploded view of CoinFT. It consists of two rigid PCBs (upper and lower sensing layers) connected with an array of silicone rubber pillars. The fPCB top shield layer provides passive shielding. The alignment tabs are removed after assembly. (c) Dimensions of each layer. The overall thickness is approximately 2 mm.

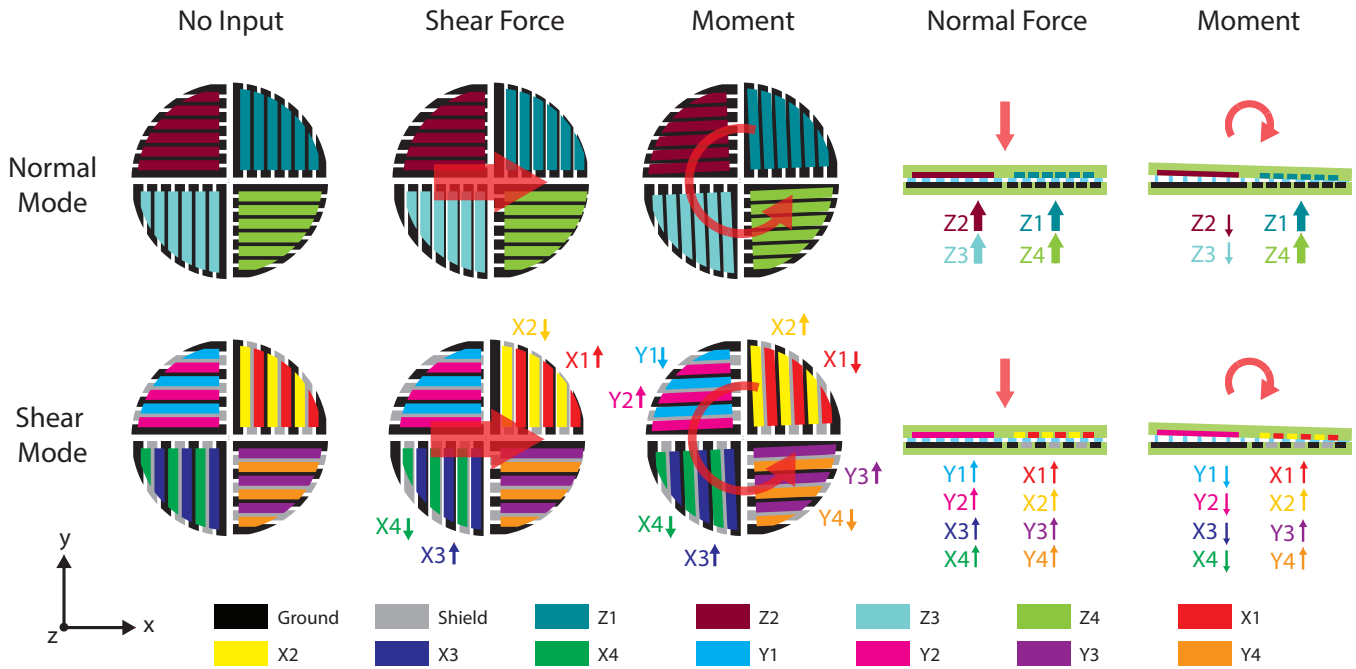


Fig. 2. CoinFT working principle. The microcontroller firmware is programmed to switch the pair of rigid PCBs between two different electrode configurations - normal mode and shear mode. The capacitance signals collected from these two configurations produce unique patterns under different force and torque inputs.

sensing layer and the lower sensing layer (Fig. 1). Capacitance is expressed as:

$$C = \frac{\epsilon A}{d} \quad (1)$$

where  $C$  is capacitance,  $\epsilon$  is the dielectric constant,  $A$  is the overlapping area of the electrodes, and  $d$  is the dis-

tance between the electrodes. The microcontroller firmware is programmed to switch the pair of rigid PCBs between two different electrode configurations every sampling sequence - normal mode and shear mode. This reconfiguration is achieved by modifying the internal electronic switches in the microcontroller, which either connect or disconnect the electrodes from

the microcontroller's capacitance-to-digital conversion (CDC) module, a technique similar to that employed by Huh et al. [18].

In the normal mode, the pair of electrodes in each quadrant in the upper sensing layer are internally connected to function as a single electrode, effectively reducing the eight physical electrodes to four:  $Z1$ ,  $Z2$ ,  $Z3$ , and  $Z4$  (Fig. 2). The two electrodes in the lower sensing layer are reconfigured to connect to *ground*. Referring to (1), this design allows the normal mode to be sensitive to inputs that changes  $d$ , such as  $F_z$ ,  $M_x$ , and  $M_y$ , but not to changes in  $A$ , which results from  $F_x$ ,  $F_y$ , and  $M_z$ . Under  $F_z$ , all normal mode electrodes ( $Z1$ ,  $Z2$ ,  $Z3$ , and  $Z4$ ) show a rise in signal, while under  $M_x$  or  $M_y$ , a differential pattern between pairs of normal mode electrodes is created (Fig. 2).

In the shear mode, electrodes in the upper sensing layer are kept as independent sensing electrodes ( $X1$ ,  $X2$ ,  $X3$ ,  $X4$ ,  $Y1$ ,  $Y2$ ,  $Y3$ , and  $Y4$ ), while the electrodes in the lower sensing layer are configured such that the *ground* and *shield* electrodes form an alternating pattern (Fig. 2). The *shield* electrode actively mitigates interference from stray capacitance by being excited to the same electrical potential as the sensing electrodes, an innate capability of PSoC™ 4100S. This design allows the shear mode to be sensitive primarily to shear inputs such as  $F_x$ ,  $F_y$ , and  $T_z$ . Under a shear pressure, the relative position of the upper sensing layer and the lower layer shifts laterally, changing  $A$  between a sensing electrode and *ground* electrode. Due to the negligible capacitance formation between a sensing electrode and a *shield* electrode, the relative position change results in a differential signal pattern in the shear mode. The comb-shaped electrodes are populated in a way that allows the first and third quadrant of the shear mode to be sensitive to loads in the  $X$  direction, while the second and fourth quadrants are sensitive to the  $Y$  direction. Under torsion ( $T_z$ ), all four quadrants in the shear mode show a differential signal pattern. Unlike the normal mode configuration where there is negligible cross-modal sensitivity by design, there is cross-coupling in the shear mode configuration. This is resolved in our calibration, as discussed in detail in Section III-D1. The unique signal pattern generated from the normal and shear mode configurations upon loads in different axes makes CoinFT a 6-axis F/T sensor.

### C. Sensor Fabrication

CoinFT is fabricated using the process illustrated in Fig. 3. A 127  $\mu\text{m}$  polyimide film pillar mask cut by a UV laser cutter (DPSS Lasers Inc., Samurai UV Marking System) is placed on an acrylic plate using dowel pins for alignment. Vacuum degassed uncured silicone rubber (TAP® Silicone RTV Mold-Making System) is smeared on the surface of the mask to fill the cavities for pillars (Fig. 3 (a)). Then, the lower sensing layer PCB primed using DOWSIL™ PR-1200 RTV Primer for enhanced adhesion is aligned and placed on the pillar mask. Another acrylic plate is placed on the assembly for equal pressure distribution and a 3.1 kg mass is added for 3 minutes to minimize the thickness of the base layer of the silicone pillars (Fig. 3 (b)). The 3 kg mass is removed, and

the pillar assembly, with a 100 g mass added, is cast inside a pressure chamber for at least 12 hours at approximately 414 kPa to compress any remaining micro-bubbles inside the silicone rubber (Fig. 3 (c)). Once the acrylic plates and the pillar mask are removed, the pillar layer is complete (Fig. 3 (d), (e)).

On the upper sensing layer PCB, after the microcontroller

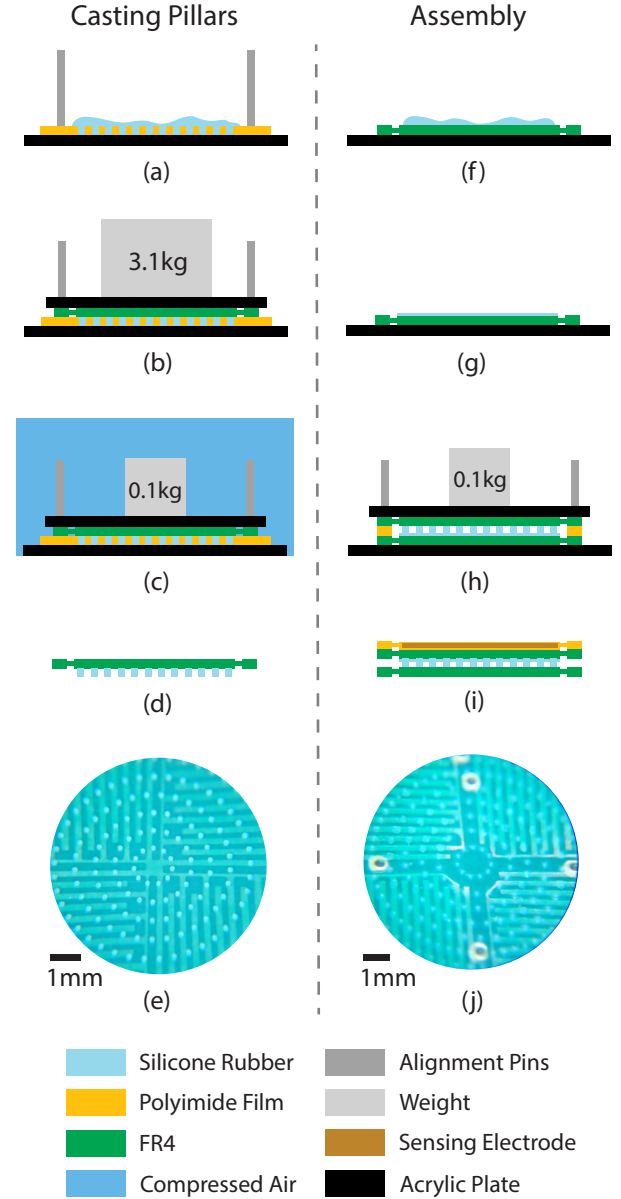


Fig. 3. The fabrication process of CoinFT. (a) Fresh uncured silicone is spread on a UV laser cut mask that is placed on an acrylic plate with alignment pins. (b) A primed lower sensing layer PCB and an acrylic plate for equal pressure distribution is stacked with a 3.1 kg weight. (c) With a 0.1 kg weight, the assembly is cured inside a pressurized chamber. (d),(e) Once the mask and acrylic plates are removed, the pillar layer is complete. (f) On a primed upper sensing layer PCB, fresh uncured silicone is spread. (g) The silicone layer is made thin and uniform through spin-coating. (h) The lower sensing layer with pillars is assembled with the upper sensing layer through precise distance control by adding spacers in between. A 0.1 kg weight and an acrylic plate for pressure distribution are added. (i) The top shield layer is attached using an adhesive. (j) A horizontal cross section of the pillar layer shows desirable bonding of the two PCB layers.

TABLE II  
BILL OF MATERIALS (BOM) FOR COINFT

Item	Quantity	Unit Cost [\$]	Total Cost [\$]
PSoC 4100S	1	3.25	3.25
Middle layer PCB	1	2.94	2.94
Top layer PCB	1	0.76	0.76
Shield PCB	1	2.09	2.09
SMD electronics	6	0.20	1.20
Molex connector	1	0.69	0.69
<b>Total</b>			<b>10.93</b>

and the electrical components are hand-soldered, the sensing area is primed and applied with vacuum degassed uncured silicone rubber (Fig. 3 (f)). Then, the silicone layer is spin-coated at 5000rpm for 75 seconds to achieve a uniform and thin layer (Fig. 3 (g)). The pillar layer is attached to the upper sensing layer PCB with a 203  $\mu\text{m}$  polyimide film spacer in between, to control the distance between the two PCBs. A 100 g mass and an acrylic plate is placed on top of the assembly to apply equally distributed pressure, ensuring that the pillars and the spun coat silicone layer are in contact (Fig. 3 (h)). The assembly is then cured inside a 65  $^{\circ}\text{C}$  oven for 72 hours. After the alignment pins and spacers are removed, the top shield layer fPCB is adhered to the other side of the upper sensing layer PCB using an adhesive (Henkel Corporation, Loctite 401 Instant Adhesive) (Fig. 3 (i)). The cross-section of the pillar assembly under a microscope is shown in Fig. 3 (j). The total cost of all components is approximately \$11, without scaled production (Table II).

#### D. Sensor Characterization

A quantitative analysis using finite element analysis (FEA) and real sample testing has been conducted to understand the behavior of CoinFT. The FEA involved a structural analysis using ANSYS (Fig. 4 (h)) to investigate the deformation of the pillar array under different loading conditions, and an electrostatics analysis in COMSOL (Fig. 4 (i)), to study the change in capacitance in the sensing electrodes resulting from pillar deformation. The pillar mechanics was modelled using a linear elastic model with a high deformation option to account for the geometric nonlinearities. The Gent model [51] was applied to convert the shore hardness of the silicone rubber into Young's modulus. With the assumption that the silicone rubber is incompressible, the effective Young's modulus of each pillar was derived using a disk model of an elastomer bonded between two plates, as modeled by Haddow and Ogden [52], shown in (2):

$$E_e = E\left(1 + \frac{1}{2}\eta^{-2}\right) \quad (2)$$

where  $E_e$  is the effective Young's modulus,  $E$  is the Young's modulus of the material, and  $\eta$  is the ratio between the height and radius of the pillars.

The dielectric constant of the silicone rubber was assumed to be 3.0, a common value for silicone rubber [53], while the dielectric constant of air was taken as 1.0. In order to verify the reliability of our FEA model, we compared the real and

TABLE III  
ACCURACY OF COINFT CALIBRATION.

Input Range: 0~5 N Normal, 0~2 N Shear						
	Fx	Fy	Fz	Mx	My	Mz
Normal+Shear (RMSE)	0.038	0.040	0.050	0.317	0.306	0.231
Shear (RMSE)	0.039	0.040	0.115	0.343	0.323	0.244
Normal+Shear ( $R^2$ )	0.994	0.994	0.997	0.995	0.995	0.992
Shear ( $R^2$ )	0.993	0.994	0.986	0.994	0.994	0.992
Input Range: 0~14 N Normal, 0~5 N Shear						
	Fx	Fy	Fz	Mx	My	Mz
Normal+Shear (RMSE)	0.186	0.134	0.186	1.114	1.322	0.810
Shear (RMSE)	0.174	0.129	0.266	1.169	1.587	0.867
Normal+Shear ( $R^2$ )	0.983	0.983	0.998	0.988	0.987	0.989
Shear ( $R^2$ )	0.979	0.985	0.996	0.986	0.981	0.986

\*\*"Normal + Shear" includes all 12 electrodes in the calibration process, while the "Shear" case uses only 8 electrodes from the shear mode. Forces errors are reported in  $N$ , and moment errors are reported in  $mNm$ . A CoinFT sample with a pillar diameter of 100  $\mu\text{m}$  was used. RMSE stands for Root Mean Squared Error.

simulated response of CoinFT to normal force (Fig. 4 (d)), where the load for the real sample was given up to 10 N at 0.1 Hz. The FEA model closely matched the actual sample response, accurately capturing the stiffening effects due to pillar deformation at higher loads, and effectively representing the behavior of CoinFT (Fig. 4 (d), (g)).

1) *CoinFT Calibration*: Based on the working principle from Fig. 2, CoinFT produces a distinguishable signal pattern from its 12 sensing electrodes (4 normal mode, 8 shear mode) under different force and torque loads. The simulated sensor response (Fig. 4 (a)-(c)) shows the distinguishable signal patterns under ideal alignment and distance of the upper and lower sensing layer PCBs. For sensor calibration, CoinFT is mounted on a commercial sensor (ATI Industrial Automation, Gamma) which provides ground truth force and torque information, while a combination of different loads are given from a human finger. The calibration procedure is purely data-driven. Ten trials, each consisting of 35 seconds of data, are used for training, and one additional trial of the same length is reserved for testing. A second-order least-squares regression is employed to map the raw capacitance signals to the corresponding force and torque values. Let  $X \in \mathbb{R}^{24 \times N}$  denote the feature matrix containing the first- and second-order capacitance terms from  $N$  samples, and let  $Y \in \mathbb{R}^{6 \times N}$  denote the corresponding reference forces and torques. The calibration matrix  $A \in \mathbb{R}^{6 \times 24}$  is obtained by solving the normal equation. The calibration results on the test set is shown in Fig. 5, and the root mean square error (RMSE) and  $R^2$  values are provided in Table III. The minimum detectable force of CoinFT is 20 mN.

The 8 shear mode electrodes respond to inputs causing change in distance,  $Fz$ ,  $Mx$ , and  $My$ , between the electrodes and the *ground* electrode (Fig. 4 (a)). While it is possible to calibrate the sensor using only the shear mode electrodes, the redundancy added by the high signal-to-noise ratio (SNR) by the normal mode signals (Fig. 4 (a)) significantly increases calibration accuracy, as shown in Table III. As expected, the increase in accuracy is more significant for  $Fz$ ,  $Mx$ , and  $My$ .

2) *Sensitivity and Dynamic Range Tuning*: Different robotic applications require varying sensor dynamic range, sensitivity, and accuracy. For instance, fine control of a

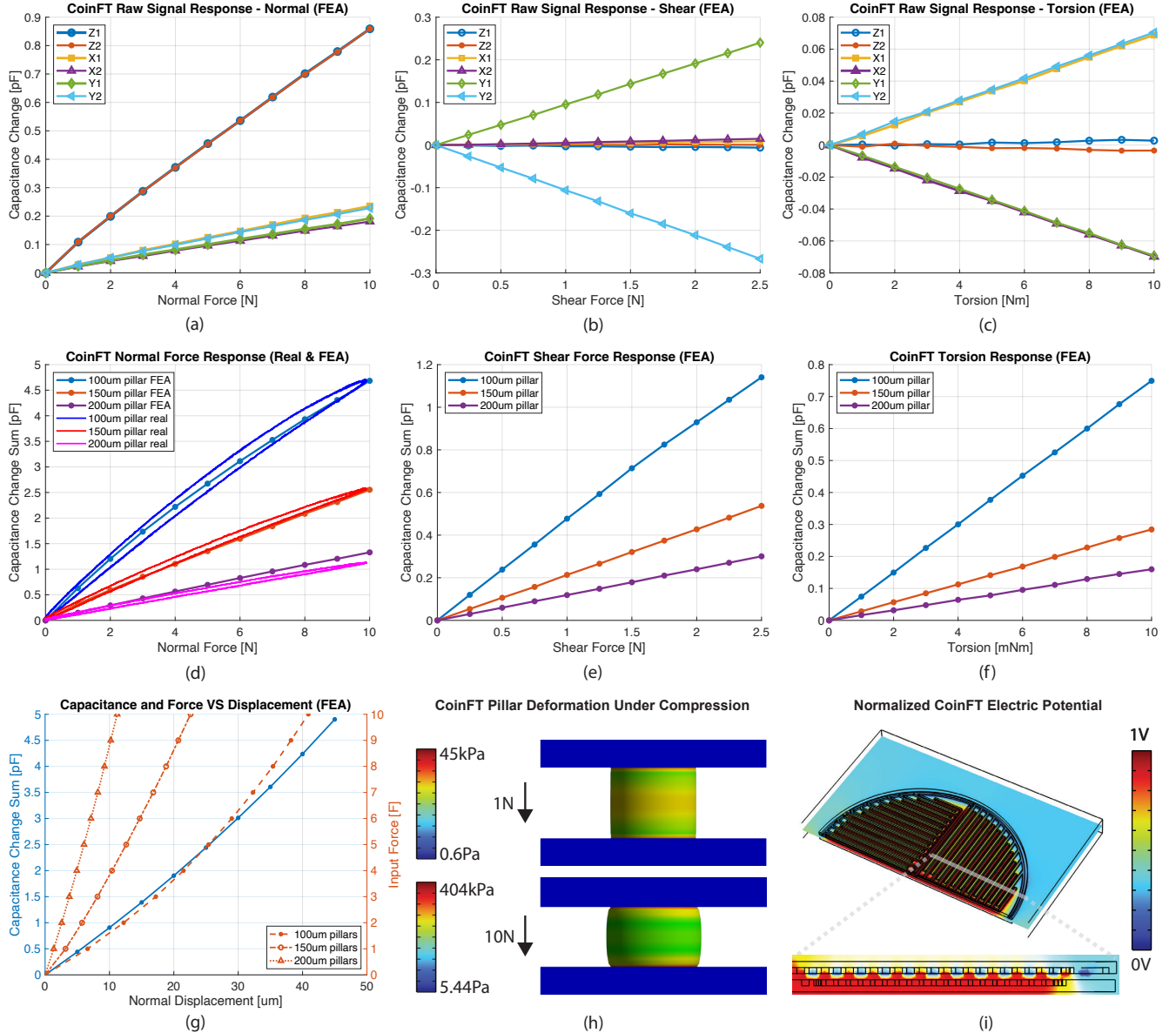


Fig. 4. CoinFT characterization using FEA. Raw capacitance response of a half of CoinFT (a) under normal force, (b) shear force, and (c) torsion. Full CoinFT response with varied pillar diameter under (d) normal force (real samples & FEA), (e) shear force (FEA), (f) and torsion (FEA). (g) Raw capacitance change with displacement and corresponding compressive force. (h) Structural modeling in FEA. (i) Electrostatics modeling in FEA.

finger-tip-mounted haptic device [54] requires high sensitivity to small forces within a dynamic range under 4 N in the normal direction, whereas an instrumented probe for ultrasound scans might require sustained loads of 20~40 N [55] and an instrumented tool for physiotherapy manipulation might require 100~200 N—with correspondingly less emphasis on sensitivity to small forces [56]. The design of the pillar layer can be adjusted to alter its mechanical properties, meeting the specific requirements of different applications.

The effect of varying pillar diameter on sensor response is illustrated in Fig. 4(d)-(g). Both experimental and FEA results demonstrate a gradual decrease in sensitivity under normal load (Fig. 4(d), (g)). This reduction in sensitivity is attributed to the stiffening of the pillars as they compress.

The constrained lateral deformation of the pillars (Fig. 4(h)) increases their stiffness, as described in equation (2). Given that the sensitivity of the capacitance change to further compression increases as shown in equation (1) and demonstrated in (Fig. 4(g)), we note that the stiffening effect is significant. For instance, the quadratic increase of stiffness and sensitivity of capacitance offset each other at lower displacements, resulting in an approximately linear capacitance–force relationship (Fig. 4(d), (g)). However, the stiffening effect outweighs the increase in capacitance change with higher deformation, explaining the decrease in sensitivity observed in Fig. 4(d).

The FEA results also illustrate that the sensitivity to changes in capacitance due to normal and shear forces, as well as torsion, is approximately inversely proportional to the cross-

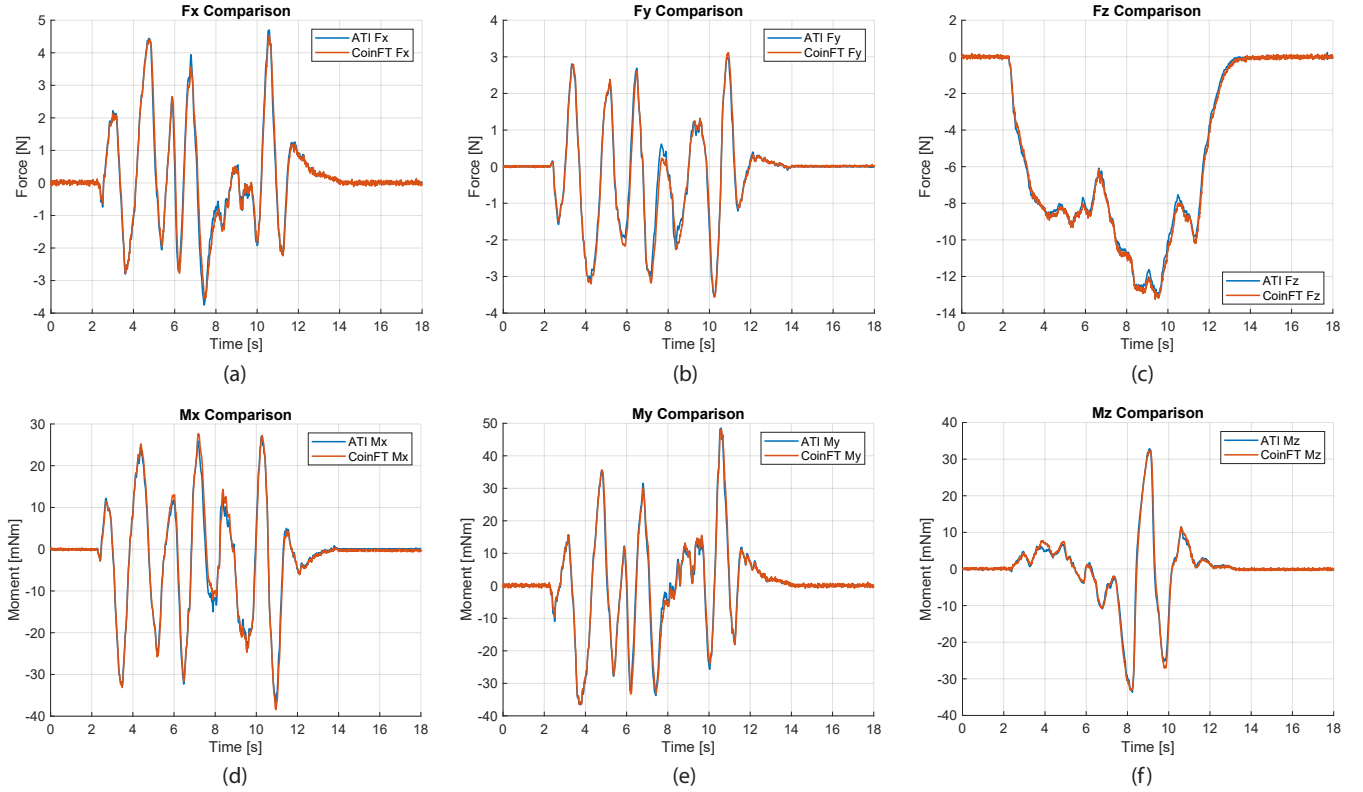


Fig. 5. Comparison of sensor readings between CoinFT and Gamma (ATI Industrial Automation) in (a) Fx, (b) Fy, (c) Fz, (d) Mx, (e) My, (f) Mz.

sectional area of the pillar array. Conversely, the dynamic range is proportional to the cross-sectional area of the pillar array.

Additional mechanical parameters that can be adjusted in the pillar layer include the number of pillars, the material selection to alter the Young's modulus, and the arrangement pattern of the pillars. Notably, the torsional stiffness can be fine-tuned while maintaining consistent normal and shear stiffness by modifying the pillar pattern, as this alters the polar moment of inertia without affecting the overall cross-sectional area of the pillar layer. This capability is particularly valuable for applications such as wearable fingertip haptic devices that require high sensitivity of both forces and torque [54].

3) *Dynamic Response*: A frequency response analysis has been conducted to investigate the mechanical bandwidth of CoinFT (Fig. 6). A dual-mode muscle lever (Aurora Scientific Inc., 309C) has been used to provide a sinusoidal force sweep either in the normal or shear directions from 0 Hz  $\sim$  120 Hz. The force input ranged from 0 N  $\sim$  2 N in the normal direction and 0.1 N  $\sim$  1.1 N in the shear direction. As shown in Fig. 6 (a), the magnitude response of CoinFT in the normal direction is kept above 70.7% (-3dB) of the input signal across the entire swept frequency. The phase lag is negligible up to 2.5 Hz, and gradually increases with higher frequency input where, at 120 Hz, the phase lag is  $-34.6^\circ$ . The magnitude response in the shear direction (Fig. 6 (b)) starts to deteriorate at 2.45 Hz and reaches 70.7% (-3dB) of the input signal at 97 Hz. At that point, the phase delay is  $-94.2^\circ$ . The cause of the phase lag is likely due to the innate hysteresis of silicone

rubber material, visible in Fig. 4 (d). These results show that the mechanical bandwidth of CoinFT is approximately 97 Hz.

4) *Robustness*: Many robot applications involve incidental large impulses that can potentially damage commercially available 6-axis F/T sensors. Due to the compliance of the pillar arrays, CoinFT demonstrates reliable robustness against impacts. As shown in Fig. 7 (a), CoinFT can accurately measure small loads of 1 N, 2 N, and 3 N even after sustaining an impact from a hammer that causes a force reading of 180 N. Such an impact would typically damage commercial sensors like the Gamma (ATI Industrial Automation) used for the CoinFT calibration. This level of robustness enables a broader range of robotic interactions beyond controlled environments, making the integration of 6-axis F/T sensors practical for real-world applications.

To further quantify the sensor's impact resistance, a controlled drop test was conducted using a 0.53 kg chrome steel ball released from a height of 0.63 m, corresponding to an impact velocity of approximately 3.5 m/s and an impact energy of 3.3 J (Fig. 7 (b)). Before and after the ten repeated impacts, the CoinFT calibration was validated under a sinusoidal loading profile of 0–5 N at 0.5 Hz using a dual-mode muscle lever (Aurora Scientific Inc., 309C). The calibration performance remained consistent, exhibiting a mean-squared error of 0.055 N and an  $R^2$  value of 0.982 when compared to the reference force. These results confirm that CoinFT maintains its measurement accuracy and structural integrity under repeated high-energy impacts.

While CoinFT exhibits strong robustness under compressive

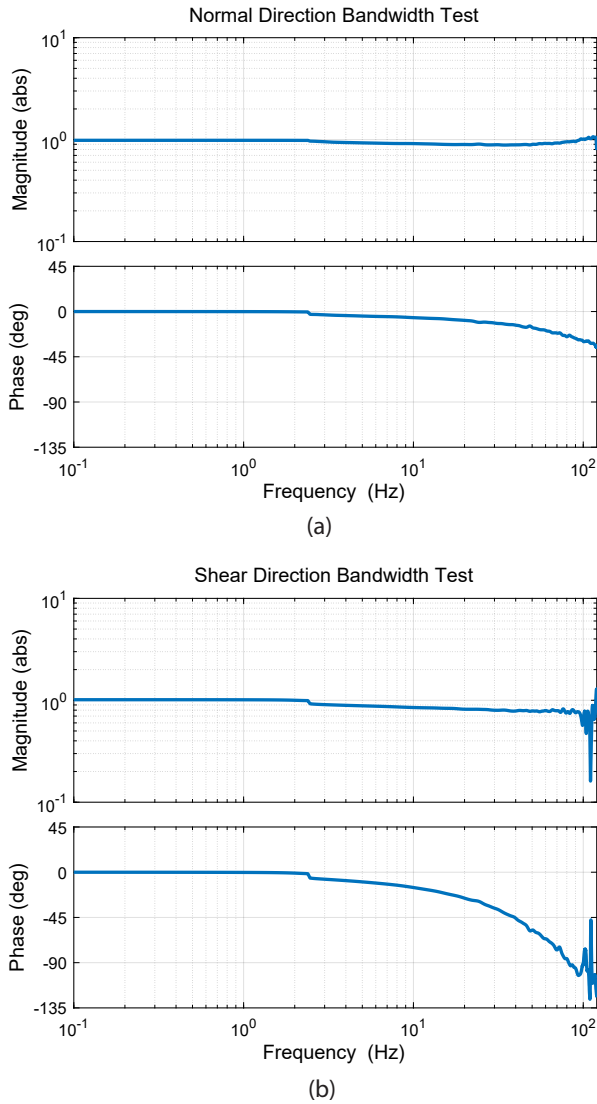


Fig. 6. CoinFT frequency response in the (a) normal and (b) shear direction.

loading, it is less robust in the tensile direction, as excessive tensile stress can cause delamination between the silicone pillars and the PCB substrate. Tensile tests conducted on five CoinFT samples showed an average ultimate tensile strength of 2.84 MPa (143 N) with a standard deviation of 1.21 MPa (61 N). Increasing the pillar diameter can increase the absolute tensile force the sensor can withstand, while improved bonding strategies, such as surface treatments or adhesive modification, are expected to further enhance the ultimate tensile strength.

5) *Thermal Effects:* We investigated the effect of temperature variation and implemented a compensation method using the on-chip temperature sensor of the PSoC. The thermal drift of the raw capacitance signals from all 12 channels was characterized in a temperature-controlled chamber. Across channels, the baseline capacitance drift was approximately 1–3% per 10,°C. This drift profile was modeled using a second-order polynomial fit, achieving  $R^2 > 0.9992$  for all channels. During inference, temperature compensation was performed by subtracting the predicted baseline drift from

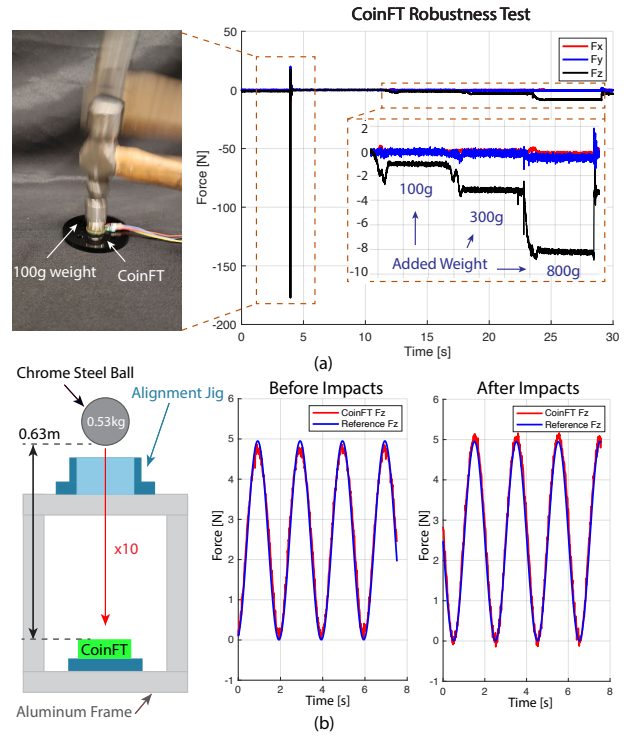


Fig. 7. CoinFT robustness evaluation. (a) CoinFT continues to provide reliable force readings even after an impact from a hammer. (b) The calibration stays consistent after ten impacts from a 0.53 kg mass dropped at a height of 0.63 m.

the raw capacitance signals prior to force/torque estimation. The ablation results under a no-load condition are shown

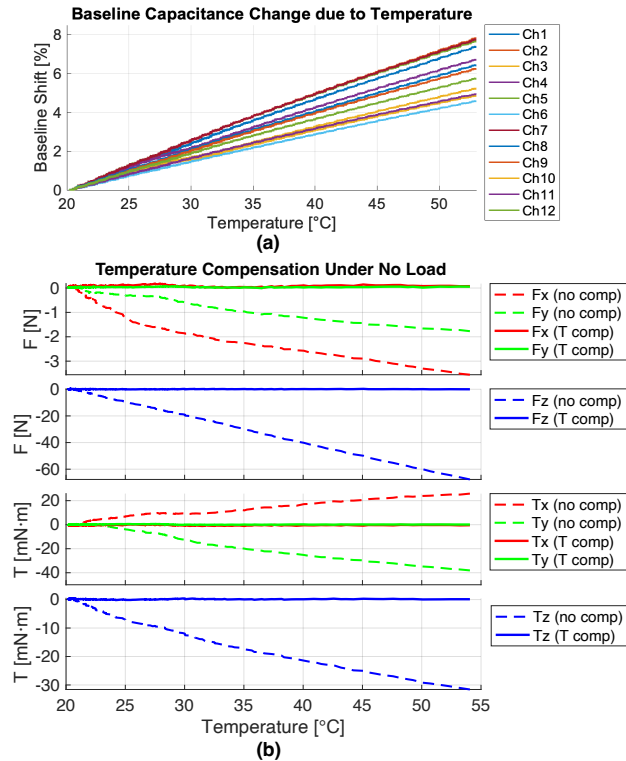


Fig. 8. Effects of temperature variation and its compensation. (a) Drift of raw signals due to temperature change. (b) Temperature compensation using an on-chip temperature sensor.

in Fig. 8. With temperature compensation, the residual force error remained below 0.4 N and torque error below 1.5 mN·m, whereas without compensation, a clear temperature-dependent drift was observed in the force readings.

#### IV. COINFT DEMONSTRATIONS

While numerous six-axis force/torque sensors have been developed, as discussed in Section II, few achieve a balance of compactness, slim form factor, low cost, accuracy, and robustness. This combination of features enables the broader adoption of F/T sensing across diverse robotic platforms. We demonstrate the versatility of CoinFT through a multi-axial contact probing setup that emulates robot fingertip interactions and an example that motivates its integration on drones.

##### A. Multi-axial Sensing for Robot Manipulators

Dexterous manipulation tasks, such as object handling or tool use, often require accurate multi-axial force/torque feedback, particularly when interactions require significant contact forces for success [57]. For integration on robot fingers, the sensing module must also maintain a compact and slim form factor to avoid drastically altering the hand geometry.

To evaluate CoinFT's performance in such settings (e.g. as in [36]), we mounted a CoinFT beneath a robot fingertip with a hemispherical dome and applied varying force and torque along multiple axes using a 7-DoF robotic arm (Flexiv Rizon 4). As shown in Fig. 9 (a), a reference force/torque sensor (ATI Gamma) was positioned beneath CoinFT to provide ground-truth measurements. The resulting data (Fig. 9 (b)) demonstrate that CoinFT achieves accuracies listed in Table IV.

TABLE IV  
MULTI-AXIAL SENSING DURING CONTACT PROBING.

	Fx	Fy	Fz	Mx	My	Mz
RMSE	0.108	0.120	0.378	5.669	3.874	0.720
$R^2$	0.994	0.995	0.999	0.993	0.996	0.986

Input range: 0~30N normal, 0~7.5N shear, 0~200 mN·m moment. Forces are reported in N, and moments in mN·m. RMSE denotes the root mean squared error, and  $R^2$  represents the coefficient of determination. A CoinFT sample with a pillar width of 300  $\mu$ m was used to account for the large input range.

##### B. Contact Force Modulation of Aerial Vehicles

Drones offer unique capabilities for performing contact-rich tasks in environments that are difficult or dangerous for humans, such as collecting biological samples from cliffs [6] or cleaning vertical surfaces [58]. However, most drones lack reliable contact sensing due to the fragility, weight, and high cost of conventional force sensors. Without such feedback, maintaining stable contact or regulating interaction forces is challenging, often resulting in unsafe or inconsistent behaviors.

CoinFT directly addresses these limitations through its compact (20 mm diameter, 2 mm thickness), lightweight (2 g, or 6.7 g including wiring and electronics), and impact-tolerant design. In this section, we demonstrate that a drone equipped with CoinFT and a simple PID-based force controller can

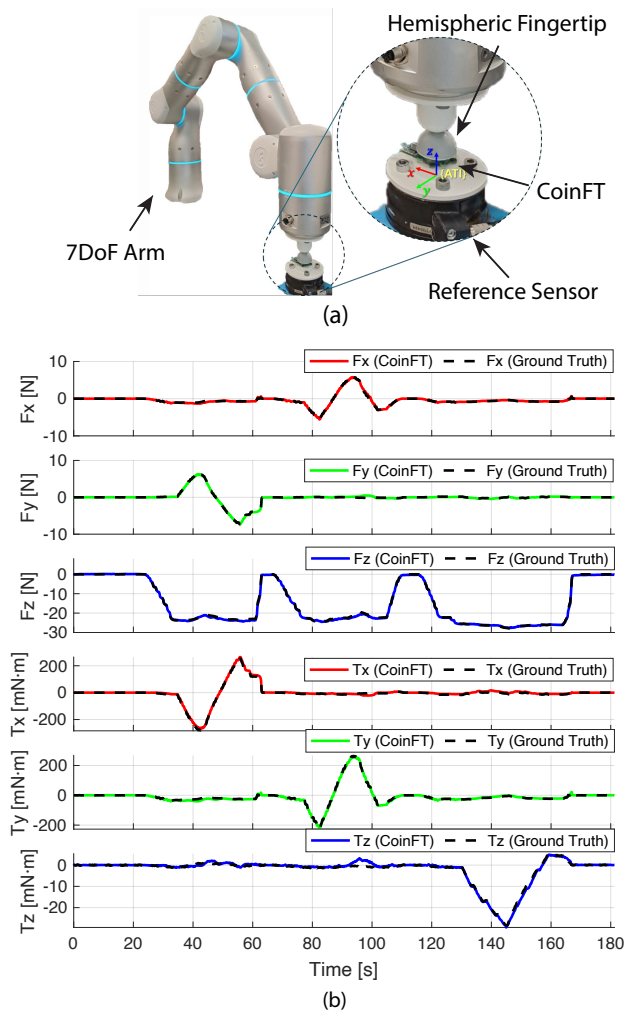


Fig. 9. Multi-axial contact probing experiment. (a) The 7DoF arm applies force and torque in different axes on a hemispherical fingertip equipped with CoinFT, approximating manipulation scenarios. (b) CoinFT and reference sensor reading comparisons. Refer to Table IV for quantitative evaluation.

safely and stably perform contact interactions, such as pressing and attaching a payload onto a surface. This experiment highlights the ease of integrating CoinFT on aerial platforms; given its low cost and mechanical resilience, the sensor can withstand or be inexpensively replaced after crashes that are common in drone operations.

While only normal force feedback was utilized in this demonstration, CoinFT's six-axis sensing capability may enable a broader range of aerial manipulation tasks, such as sliding, scraping, or compliant alignment that would not be feasible without multi-axial sensing.

1) *Drone with CoinFT*: Our drone is a 127 mm frame quadrotor with an UpBoard companion computer and a PixRacer flight controller (Fig. 10). CoinFT is attached at the distal tip of a custom mount, which is connected in series with the proximal mount through a telescoping mechanism with rubber bands (Fig. 10(c)). The compliant element in series helps to reduce impact upon contact and simplify control. CoinFT is connected to the UpBoard computer through a USB port. A socket is attached at the top of CoinFT which allows

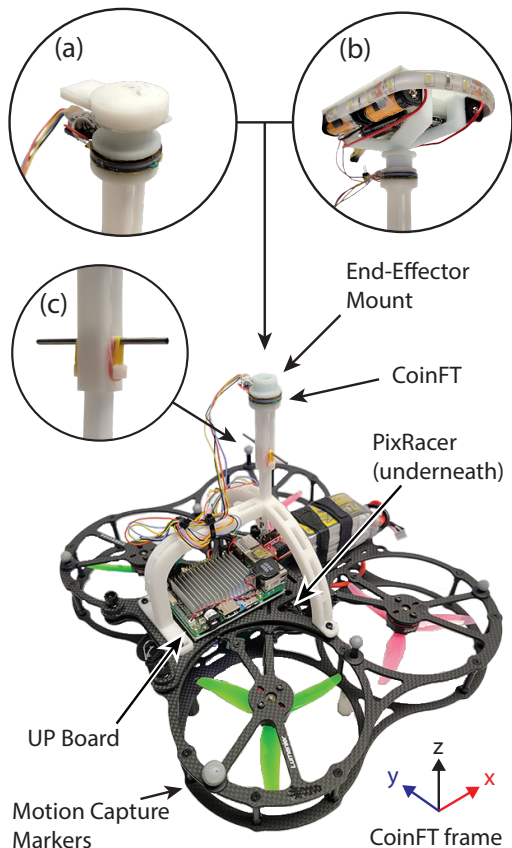


Fig. 10. Experimental setup for drones performing contact rich tasks. Different end-effectors can be attached to the CoinFT mount, such as (a) a tip for general contact or (b) a package of electronics to be attached on a surface. Compliance is added in series through a (C) telescoping mechanism with pre-tensioned rubber bands to mitigate impact upon contact.

mounting different end-effectors for different tasks, such as a round tip for general contact or a package of electronics (Fig. 10(a) and (b)). The electronics package consists of an ESP32 microcontroller that uses four 12 V batteries in parallel to control a strip of LEDs to signal successful package deployment. Pressure sensitive adhesives are attached at the corners on the top side of the package. Since the package is not mechanically attached to the socket, the package will attach to a surface once sufficient pressure provides the necessary adhesion.

2) *Attitude Controller for Contact*: To simulate an unstructured environment, we designed a controller for the quadrotor that does not explicitly know the height of the contact surface, thus relying on CoinFT not only to execute force modulation but also to find the contact surface.

Given that the focus here is control with respect to contact, we simplify the navigation aspect of the control problem by providing the drone with accurate estimates of its pose and orientation via an external motion capture system. We then use this as feedback to track a minimum snap trajectory spline [59] to a region near the contact surface. We do not provide the drone with the actual height of the contact surface. Instead, our policy will search through a range of heights within which we are confident that the contact surface exists and transform it into a sequence of desired positions ( $\mathbf{p}_{des}$ ), velocities ( $\mathbf{v}_{des}$ )

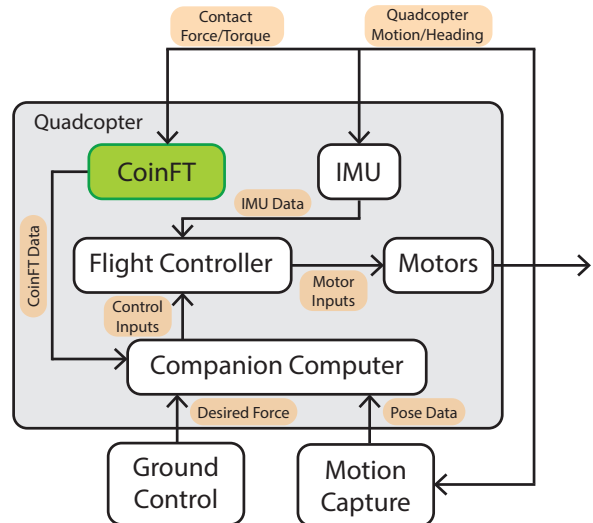


Fig. 11. System diagram of the integrated drone test setup.

and orientations ( $\mathbf{q}_{des}$ ), for our controller to track while it searches for contact.

We interface with the PixRacer at the attitude control level, comprising of a commanded normalized thrust force ( $\hat{f}_{cmd}$ ) and a commanded orientation ( $\mathbf{q}_{cmd}$ ). We choose this level of control as it allows us to guarantee that the drone is stationary and perpendicular to the contact surface (through commanded orientation) and gives us direct control of the thrust for force modulation.

To account for the drone flight envelope including both in-contact and out-of-contact flight, we use a switching, cascaded PID controller to advance from currently observed states  $[\mathbf{p}_{obs} \ \mathbf{v}_{obs} \ \mathbf{q}_{obs}]$  to desired attitude commands  $\mathbf{u}_{cmd}$ . We start by taking the position and velocity error:

$$\mathbf{e}_p = \mathbf{p}_{obs} - \mathbf{p}_{des}, \quad \mathbf{e}_v = \mathbf{v}_{obs} - \mathbf{v}_{des}$$

from which we compute a desired force vector while accounting for gravity:

$$\mathbf{F}_{des} = -\mathbf{K}_p \mathbf{e}_p - \mathbf{K}_v \mathbf{e}_v - m\mathbf{g}$$

where  $\mathbf{F}_{des}$  is the desired force,  $m$  is the mass of the drone,  $\mathbf{g}$  is the gravity vector, and  $(\mathbf{K}_p, \mathbf{K}_v)$  are positive definite gain matrices that switch between in-contact gains and out-of-contact gains:

$$\mathbf{K}_p, \mathbf{K}_v = \begin{cases} \mathbf{K}_p^{oc}, \mathbf{K}_v^{oc} & \text{if out of contact} \\ \mathbf{K}_p^{ic}, \mathbf{K}_v^{ic} & \text{if in contact} \end{cases}$$

Using the quaternion to rotation matrix to basis vector mapping  $\mathbf{q}_i \iff \mathbf{R}_i \iff [x_i \ y_i \ z_i]$  on both the desired orientation ( $\mathbf{q}_{des}$ ) and commanded orientation ( $\mathbf{q}_{cmd}$ ), we can compute the latter:

$$\begin{aligned} z_{cmd} &= \frac{\mathbf{F}_{des}}{\|\mathbf{F}_{des}\|} \\ y_{cmd} &= \frac{z_{cmd} \times \mathbf{x}_{des}}{\|z_{cmd} \times \mathbf{x}_{des}\|} \\ x_{cmd} &= y_{cmd} \times z_{des} \end{aligned}$$

To get the commanded normalized thrust force we start by getting a desired normalized thrust ( $\hat{f}_{des}$ ). This is done by invoking the quaternion to basis vector mapping to get  $\mathbf{z}_{obs}$  from  $\mathbf{q}_{obs}$  and then projecting the desired force vector onto it:

$$\begin{aligned} \mathbf{f}_{des} &= \mathbf{F}_{des} \cdot \mathbf{z}_{obs} \\ \hat{f}_{des} &= k_f f_{des} \end{aligned}$$

where  $k_f$  is the thrust normalization coefficient that can be empirically approximated from prior flights. This is then fed into a state machine (Algorithm 1) for thrust control that switches modes during contact events and tracks desired contact forces using CoinFT feedback. The two key features of the state machine is a linear search function for the contact force and a PID tracking controller. The former enables graceful transitions when the initial desired contact force is large while the latter not only enables us to hold but also track a changing desired contact force. Combined, these allow for more consistent and safer performance. Given an observed force on CoinFT ( $f_{oc}$ ), desired force on CoinFT ( $f_{dc}$ ) and current time ( $t_{cr}$ ) we perform the steps in Algorithm 1 to get the commanded normalized thrust. Assuming compressive force, we use the absolute values of the CoinFT reading in the normal direction.

---

#### Algorithm 1 Thrust State Machine and PID Controller

---

```

1: Inputs:  $\hat{f}_{des}, f_{oc}, f_{dc}, t_{cr}$ 
2: Outputs:  $\hat{f}_{cmd}, S$ 
3: Parameters: Force Increment  $\Delta f$ , Proportional Gain  $k_p$ ,
   Integral Gain  $k_i$ , Derivative Gain  $k_d$ , Hold Duration  $T$ 
4: Initialization:
5:  $e_{prev} \leftarrow 0, \int e dt \leftarrow 0, \hat{f}_{cmd} \leftarrow \hat{f}_{des}, S \leftarrow \text{FREE}$ 
6: if S is FREE then
7:    $\hat{f}_{cmd} \leftarrow \hat{f}_{des}$ 
8:   if  $f_{oc} > 0$  then
9:      $S \leftarrow \text{SEARCH}$ 
10: else if S is SEARCH then
11:    $\hat{f}_{cmd} \leftarrow \hat{f}_{cmd} + \Delta f$ 
12:   if  $f_{oc} \geq f_{dc}$  then
13:      $f_{hold} \leftarrow \hat{f}_{cmd}, t_{prev} \leftarrow t_{cr}, t_0 \leftarrow t_{cr}$ 
14:      $S \leftarrow \text{HOLD}$ 
15: else if S is HOLD then
16:    $\Delta t \leftarrow t_{cr} - t_{prev}, e_{curr} \leftarrow f_{oc} - f_{dc}$ 
17:    $P \leftarrow k_p e_{curr}, I \leftarrow I + k_i e_{curr} \Delta t, D \leftarrow k_d \frac{e_{curr} - e_{prev}}{\Delta t}$ 
18:    $\hat{f}_{cmd} \leftarrow f_{hold} + P + I + D$ 
19:    $e_{prev} \leftarrow e_{curr}$ 
20:   if  $t_{cr} - t_0 \geq T$  then
21:     break

```

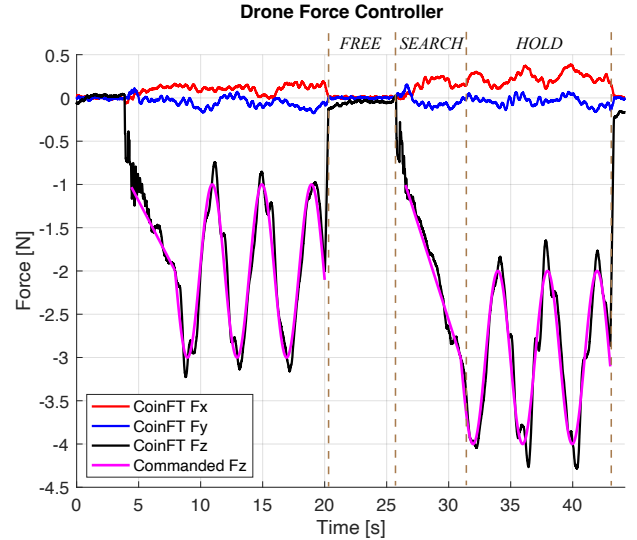
---

The CoinFT feedback data lets us use the state machine to dynamically switch the gain matrices  $\mathbf{K}_p, \mathbf{K}_v$  where we use the out of contact gains when in FREE state and in contact gains otherwise (Algorithm 1).

3) *Force Controlled Deployment of Objects on Environment Surfaces:* To test the designed force controller and perform electronics package delivery tasks, we conducted flight tests. The test setup includes a laser-cut acrylic plate horizontally



(a)



(b)

Fig. 12. Results of the force controller test. (a) The drone ascends until contact is made with the test setup, where it initiates force control. (b) CoinFT readings and commanded force.

attached to a structure made of extruded aluminum frames (Fig. 12 (a)), simulating an environmental surface. The integrated system consists of a ground control station (PC), motion capture system (OptiTrack, NaturalPoint, Inc.), and a drone equipped with a companion computer, flight controller, IMU, and a CoinFT (Fig. 11). The proposed attitude controller runs on the companion computer at 20 Hz, providing control inputs to the flight controller, which then converts these inputs into PWM signals for the four motors.

The performance of the proposed attitude-based force controller is illustrated in Fig. 12(b). A hemispherical contact tip (Fig. 10 (a)) is mounted on the drone. During the *FREE* state, the drone ascends until contact is sensed. In the *SEARCH* state, the thrust is linearly ramped up until a desired contact force is reached, which is initially set by the ground control station. The controller then transitions to the *HOLD* state, where it tracks a pre-programmed sinusoidal force command. The force controller demonstrates accurate tracking, with an RMS error of 0.1779 N. During flight tests, CoinFT showed no noticeable increase in noise or degradation in signal quality despite the potential electromagnetic interference from the motors [60], thanks to the effectiveness of its shielding design.

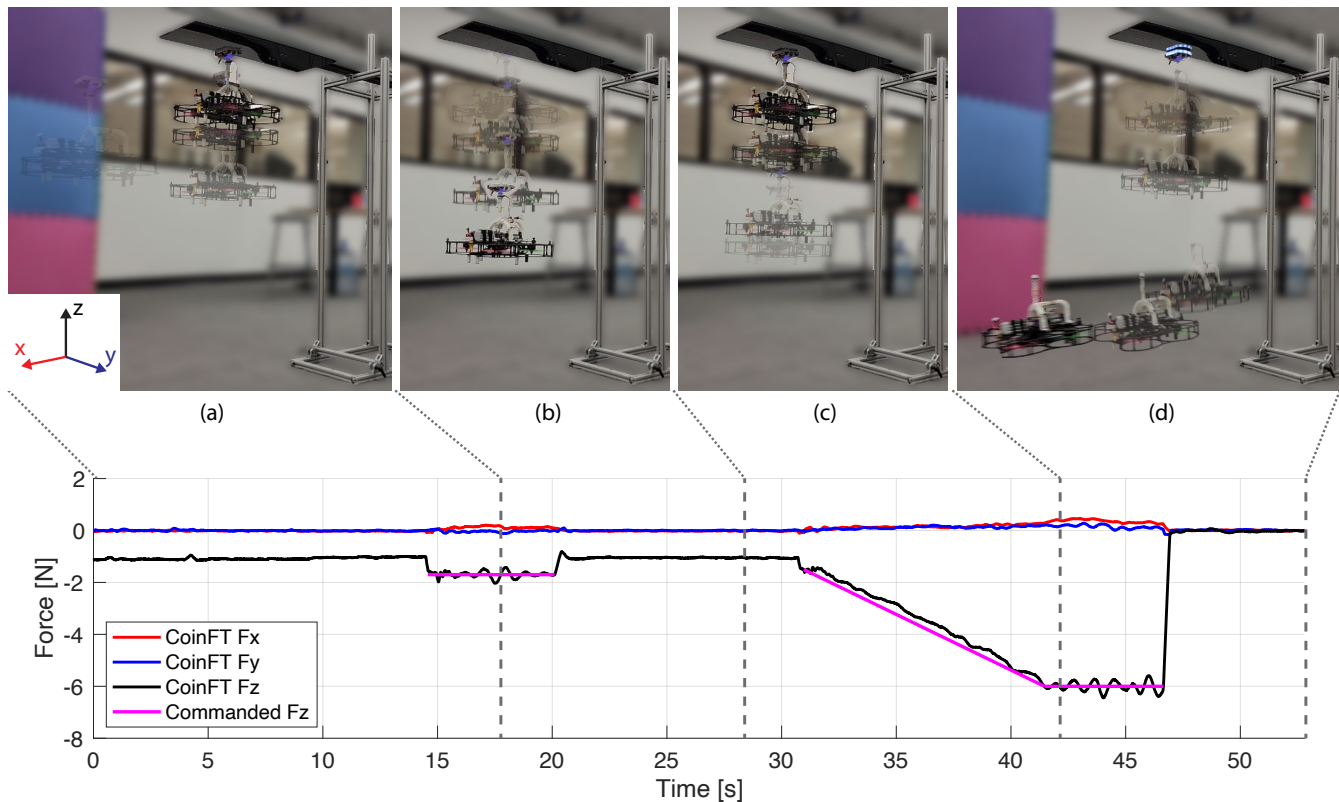


Fig. 13. Drone attaching a package of electronics on environment surfaces using force control. (a) The drone gently presses the package on the horizontal surface. (b) After descending, it still feels the weight of the package through CoinFT. (c) The drone presses the package with a larger force on the surface. (d) Upon descent, it no longer feels the weight of the package. It turns on the package and leaves the scene.

Using the force controller, the drone can attach electronics packages to environmental surfaces such as a tree branch by applying a range of force—sufficient to complete the task but not sufficient to damage the environment, or expend more energy than required. The electronics package, equipped with pressure-sensitive adhesives and weighing 95 g (Fig. 10 (b)), is mounted on the drone. Adequate pressure must be applied for the package to adhere securely to a surface. The drone initially hovers below the horizontal surface and ascends until contact is detected. Upon contact, the contact force ramps up to a commanded value of 0.7 N, which registers as approximately 1.7 N in CoinFT due to the package’s weight (Fig. 13 (a)). The drone breaks contact and descends while still sensing approximately 1 N in CoinFT, detecting that the package has not adhered properly (Fig. 13 (b)). The drone then autonomously increases the desired contact force to 5 N (Fig. 13 (c)). After applying the higher force, the drone no longer senses the package’s weight through CoinFT and sends an *ON* command to the electronics package via WiFi, activating the LEDs to signal task success (Fig. 13 (d)). These precisely controlled interactions are valuable for attaching objects, such as sensor packages, to potentially fragile surfaces like tree branches or for performing general force-controlled tasks, such as cleaning windows on tall buildings.

## V. DISCUSSION & FUTURE WORK

While this paper demonstrates CoinFT’s capabilities in contact probing or drone platforms, the sensor’s versatility extends to a wide range of other robotic applications. CoinFT has already been used in wearable haptic devices, where it measures and controls the contact force between the device and the human subject. Sarac et al. [35] used CoinFT to reveal that people perceive different intensities when the same force is applied in normal versus shear directions. Yoshida et al. [7] employed CoinFT to ensure consistency in user studies by initializing the haptic device factor based on contact force rather than position. This approach is crucial for accommodating variations in users’ body shapes, as position-based initialization does not consistently deliver uniform haptic feedback. CoinFT’s slim and compact design also makes it highly suitable for wearable fingertip devices [54].

CoinFT has also been directly attached to the fingertips of a commercial anthropomorphic robot hand [36] for learning force-informed actions from kinesthetic demonstrations. In such setup, it can sense contact force for controlled, forceful interaction or track the contact point by utilizing force and torque information for intrinsic tactile sensing [61]. When connected via I2C communication, multiple CoinFTs can be integrated to sensorize all fingers at the same 360 Hz sampling rate, enhancing the robot hand’s ability to perform fine-manipulation tasks. Its low cost and robustness against incidental impacts make CoinFT particularly desirable for robot

hands operating in unstructured and cluttered environments.

While the current form factor of CoinFT has been designed to showcase its versatility across various robotic platforms such as drones, robot fingertips, and haptic devices, it can be tailored to meet the specific needs of other applications. For example, CoinFT can be made even narrower to sensorize compact medical devices [62]. The tradeoff in this case would be a decrease in sensitivity due to the reduced sensing area. Conversely, CoinFT could be scaled up to fit the form factor of quadruped or humanoid feet, allowing for the measurement of ground reaction forces (GRF). The larger sensing area in this configuration would enable both higher sensitivity and an expanded dynamic range. This would require a careful selection of design parameters to meet the specifications on sensitivity and dynamic range, as discussed in Section III-D. Moreover, the dual-mode electrode-switching strategy used in CoinFT may also inspire future capacitive tactile sensors for enhancing multi-axial sensitivity, particularly those employing programmable capacitance sensing microcontrollers that permit low-level reconfiguration of electrode connections.

While CoinFT is versatile and suitable for a wide range of robotic applications, it is not intended as a direct replacement for existing commercial sensors like the Gamma (ATI Industrial Automation). The mechanical bandwidth of CoinFT is an order of magnitude lower than that of the Gamma (1 kHz), making it less capable of detecting highly dynamic contacts. Additionally, the Gamma offers a finer force resolution even with its high dynamic response capabilities.

Other challenges must be considered when using CoinFT. While shielding has been implemented to prevent the coupling of stray capacitance, the surface-mounted electrodes of the chip remain partially exposed, which can result in imperfect shielding. While elastomer creep can affect signal, its effect is expected to be small in most applications. The silicone rubber used in CoinFT is a tin-cured RTV elastomer with mechanical properties similar to that in [48]. As noted then, it has low hysteresis and creep in comparison to other elastomers (e.g. urethanes) of similar stiffness. More detailed characterization of similar silicone materials can be found in [49], [50], [63], [64]. For example, the material in [64] showed reversible viscoelastic recovery under loads up to 0.5 MPa, which would correspond to  $\sim 32$  N on CoinFT—suggesting that no permanent creep or damage occurs after repeated loading. Consequently, in applications that do not sustain a large load for long periods of time, mechanical creep is expected to contribute negligibly to signal drift, and recalibration or sensor replacement will not be required.

The current thin PCB might not be entirely rigid and could deform out of plane under significant local pressure, potentially reducing calibration accuracy. This issue, however, can be mitigated by using a slightly thicker PCB or bonding a thin layer of stiff material. Despite the limitations, CoinFT remains valuable for many robotic applications where such high precision and bandwidth in a 6-axis F/T sensor is not essential, and where robustness and low cost are prioritized.

The proposed attitude control strategy is expected to be effective only in the directions where the drone is fully actuated. Through experimentation, we have observed that

precise force control in the lateral direction is challenging with a quadrotor due to the coupling between tilt and lateral displacement. However, CoinFT and the proposed controller can be valuable for modulating lateral contact force when using a fully actuated drone [12], [44].

## VI. CONCLUSION

In this paper, we introduced CoinFT, a coin-sized capacitive 6-axis F/T sensor composed of a pair of specially designed PCBs connected by an array of silicone rubber pillars. Through a comprehensive characterization, CoinFT has demonstrated a unique combination of compactness, robustness, affordability, and reliable performance. These qualities make it an ideal solution for various robotic applications, including drones, robot hands, and wearable haptic devices, particularly in real-world scenarios where large incidental impulses are common.

While CoinFT offers considerable versatility, it is not intended as a replacement for commercially available 6-axis F/T sensors, which typically offer a larger dynamic range, finer force resolution, and higher bandwidth. Instead, CoinFT excels in applications where such high-end specifications are not a priority, while low cost and scalable deployment are desirable.

We demonstrated the utility of CoinFT by a multi-axial contact probing experiment emulating fingertip-scale interactions, and integrating it with a drone to perform force-controlled tasks, such as attaching an electronics package to environmental surfaces. This capability is an example of CoinFT's potential to democratize the use of 6-axis F/T sensors across a broad range of robotic platforms, enabling more widespread adoption in applications that demand robustness and cost-effectiveness without sacrificing essential functionality. To promote this use of CoinFT technology, we have published solid models, fabrication instructions and software as an open-source design at <https://coin-ft.github.io/>.

## ACKNOWLEDGEMENTS

Meta Reality Labs Research, Toyota Research Institute, and the Kwanjeong Fellowship provided funds to support this work. The authors thank Claire Chen, Kyle Yoshida, Crystal Winston, Mine Sarac, and Alice Wu for exciting and insightful discussions about CoinFT applications.

## REFERENCES

- [1] H. T. Suh, N. Kuppusswamy, T. Pang, P. Mitiguy, A. Alspach, and R. Tedrake, "Seed: Series elastic end effectors in 6d for visuotactile tool use," in *IEEE/RSJ International Conference on Intelligent Robots and Systems*, 2022, pp. 4684–4691.
- [2] R. Song, F. Li, W. Quan, X. Yang, and J. Zhao, "Skill learning for robotic assembly based on visual perspectives and force sensing," *Robotics and Autonomous Systems*, vol. 135, p. 103651, 2021.
- [3] J. Konstantinova, G. Cotugno, P. Dasgupta, K. Althoefer, and T. Nanayakkara, "Autonomous robotic palpation of soft tissue using the modulation of applied force," in *IEEE International Conference on Biomedical Robotics and Biomechanics*, 2016.
- [4] P. M. Grice, M. D. Killpack, A. Jain, S. Vaish, J. Hawke, and C. C. Kemp, "Whole-arm tactile sensing for beneficial and acceptable contact during robotic assistance," in *2013 IEEE 13th International Conference on Rehabilitation Robotics*, 2013, pp. 1–8.
- [5] M. A. Lin, R. Thomasson, G. Uribe, H. Choi, and M. R. Cutkosky, "Exploratory hand: Leveraging safe contact to facilitate manipulation in cluttered spaces," *IEEE Robotics and Automation Letters*, vol. 6, no. 3, pp. 5159–5166, 2021.
- [6] H. La Vigne, G. Charron, J. Rachiele-Tremblay, D. Rancourt, B. Nyberg, and A. Lussier Desbiens, "Collecting critically endangered cliff plants using a drone-based sampling manipulator," *Scientific Reports*, vol. 12, no. 1, 2022.
- [7] K. T. Yoshida, Z. A. Zook, H. Choi, M. Luo, M. K. O'Malley, and A. M. Okamura, "Design and evaluation of a 3-dof haptic device for directional shear cues on the forearm," *IEEE Transactions on Haptics*, pp. 1–13, 2024.
- [8] M. Y. Cao, S. Laws, and F. R. y. Baena, "Six-axis force/torque sensors for robotics applications: A review," *IEEE Sensors Journal*, vol. 21, no. 24, pp. 27238–27251, 2021.
- [9] K. Shaw, A. Agarwal, and D. Pathak, "Leap hand: Low-cost, efficient, and anthropomorphic hand for robot learning," 2023. [Online]. Available: <https://arxiv.org/abs/2309.06440>
- [10] J. W. Guggenheim, L. P. Jentoft, Y. Tenzer, and R. D. Howe, "Robust and inexpensive six-axis force-torque sensors using mems barometers," *IEEE/ASME Transactions on Mechatronics*, vol. 22, no. 2, pp. 838–844, 2017.
- [11] T. G. Chen, K. A. W. Hoffmann, J. E. Low, K. Nagami, D. Lentink, and M. R. Cutkosky, "Aerial grasping and the velocity sufficiency region," *IEEE Robotics and Automation Letters*, vol. 7, no. 4, pp. 10009–10016, 2022.
- [12] X. Guo, G. He, M. Mousaei, J. Geng, G. Shi, and S. Scherer, "Aerial interaction with tactile sensing," 2023. [Online]. Available: <https://arxiv.org/abs/2310.00142>
- [13] S. S. Kumar and B. D. Pant, "Design principles and considerations for the 'ideal' silicon piezoresistive pressure sensor: a focused review," *Microsystem Technologies*, vol. 20, no. 7, p. 1213–1247, 2014.
- [14] S. Stassi, V. Cauda, G. Canavese, and C. Pirri, "Flexible tactile sensing based on piezoresistive composites: A review," *Sensors*, vol. 14, no. 3, p. 5296–5332, 2014.
- [15] R. Ouyang and R. Howe, "Low-cost fiducial-based 6-axis force-torque sensor," in *International Conference on Robotics and Automation*, 2020, pp. 1653–1659.
- [16] U. Kim, H. Jeong, H. Do, J. Park, and C. Park, "Six-axis force/torque fingertip sensor for an anthropomorphic robot hand," *IEEE Robotics and Automation Letters*, vol. 5, no. 4, pp. 5566–5572, 2020.
- [17] A. El-Azizi, S. Islam, P. Piacenza, K. Jiang, I. Kymissis, and M. Ciocarlie, "Compact led-based displacement sensing for robot fingers," 2025. [Online]. Available: <https://arxiv.org/abs/2410.03481>
- [18] T. M. Huh, H. Choi, S. Willcox, S. Moon, and M. R. Cutkosky, "Dynamically reconfigurable tactile sensor for robotic manipulation," *IEEE Robotics and Automation Letters*, vol. 5, no. 2, pp. 2562–2569, 2020.
- [19] A. Berman, K. Hsiao, S. E. Root, H. Choi, D. Ilyn, C. Xu, E. Stein, M. Cutkosky, J. M. DeSimone, and Z. Bao, "Additively manufactured micro-lattice dielectrics for multiaxial capacitive sensors," *Science Advances*, vol. 10, no. 40, p. eadq8866, 2024.
- [20] X. A. Wu, S. A. Suresh, H. Jiang, J. V. Ulmen, E. W. Hawkes, D. L. Christensen, and M. R. Cutkosky, "Tactile sensing for gecko-inspired adhesion," in *IEEE/RSJ International Conference on Intelligent Robots and Systems*, 2015, pp. 1501–1507.
- [21] N. Yao and S. Wang, "Recent progress of optical tactile sensors: A review," *Optics & Laser Technology*, vol. 176, p. 111040, 2024.
- [22] O. Al-Mai, M. Ahmadi, and J. Albert, "Design, development and calibration of a lightweight, compliant six-axis optical force/torque sensor," *IEEE Sensors Journal*, vol. 18, no. 17, pp. 7005–7014, 2018.
- [23] L. Xiong, Y. Guo, G. Jiang, X. Zhou, L. Jiang, and H. Liu, "Six-dimensional force/torque sensor based on fiber bragg gratings with low coupling," *IEEE Transactions on Industrial Electronics*, vol. 68, no. 5, pp. 4079–4089, 2021.
- [24] S. Zhang, Z. Chen, Y. Gao, W. Wan, J. Shan, H. Xue, F. Sun, Y. Yang, and B. Fang, "Hardware technology of vision-based tactile sensor: A review," *IEEE Sensors Journal*, vol. 22, no. 22, pp. 21410–21427, 2022.
- [25] W. K. Do, B. Jurewicz, and M. Kennedy, "Densetact 2.0: Optical tactile sensor for shape and force reconstruction," in *IEEE International Conference on Robotics and Automation*, 2023, pp. 12549–12555.
- [26] B. Ward-Cherrier, N. Pestell, L. Cramphorn, B. Winstone, M. E. Giannaccini, J. Rossiter, and N. F. Lepora, "The tactip family: Soft optical tactile sensors with 3d-printed biomimetic morphologies," *Soft Robotics*, vol. 5, no. 2, pp. 216–227, 2018.
- [27] W. Yuan, S. Dong, and E. Adelson, "Gelsight: High-resolution robot tactile sensors for estimating geometry and force," *Sensors*, vol. 17, no. 12, p. 2762, 2017.
- [28] M. Lambeta, T. Wu, A. Sengul, V. R. Most, N. Black, K. Sawyer, R. Mercado, H. Qi, A. Sohn, B. Taylor *et al.*, "Digitizing touch with an artificial multimodal fingertip," *arXiv preprint arXiv:2411.02479*, 2024.
- [29] W. Li, M. Wang, J. Li, Y. Su, D. K. Jha, X. Qian, K. Althoefer, and H. Liu, "L<sup>3</sup> f-touch: A wireless gelsight with decoupled tactile and three-axis force sensing," *IEEE Robotics and Automation Letters*, vol. 8, no. 8, pp. 5148–5155, 2023.
- [30] W. Li, A. Alomainy, I. Vitanov, Y. Noh, P. Qi, and K. Althoefer, "F-touch sensor: Concurrent geometry perception and multi-axis force measurement," *IEEE Sensors Journal*, vol. 21, no. 4, pp. 4300–4309, 2021.
- [31] D. Baimukashev, Z. Kappasov, and H. A. Varol, "Shear, torsion and pressure tactile sensor via plastic optofiber guided imaging," *IEEE Robotics and Automation Letters*, vol. 5, no. 2, pp. 2618–2625, 2020.
- [32] Y.-j. Li, X.-s. Xu, G.-c. Wang, S.-k. Cao, N.-j. Chen, and X. Sun, "Fault-tolerant measurement mechanism research on pre-tightened four-point supported piezoelectric six-dimensional force/torque sensor," *Mechanical Systems and Signal Processing*, vol. 135, p. 106420, 2020.
- [33] D. G. Black, A. Hossein Hadi Hosseinabadi, N. Rangga Pradnyawira, M. Nogami, and S. E. Salcudean, "Low-profile 6-axis differential magnetic force/torque sensing," *IEEE Transactions on Medical Robotics and Bionics*, vol. 6, no. 3, pp. 992–1003, 2024.
- [34] H. Choi, D. Brouwer, M. A. Lin, K. T. Yoshida, C. Rognon, B. Stephens-Fripp, A. M. Okamura, and M. R. Cutkosky, "Deep learning classification of touch gestures using distributed normal and shear force," *International Conference on Intelligent Robots and Systems*, pp. 3659–3665, 2022.
- [35] M. Sarac, T. M. Huh, H. Choi, M. R. Cutkosky, M. D. Luca, and A. M. Okamura, "Perceived intensities of normal and shear skin stimuli using a wearable haptic bracelet," *IEEE Robotics and Automation Letters*, vol. 7, no. 3, pp. 6099–6106, 2022.
- [36] C. Chen, Z. Yu, H. Choi, M. Cutkosky, and J. Bohg, "Dexforce: Extracting force-informed actions from kinesthetic demonstrations for dexterous manipulation," 2025. [Online]. Available: <https://arxiv.org/abs/2501.10356>
- [37] M. R. Rezaee, N. A. W. A. Hamid, M. Hussin, and Z. A. Zukarnain, "Comprehensive review of drones collision avoidance schemes: Challenges and open issues," *IEEE Transactions on Intelligent Transportation Systems*, vol. 25, no. 7, pp. 6397–6426, 2024.
- [38] J. Meng, J. Buzzatto, Y. Liu, and M. Liarokapis, "On aerial robots with grasping and perching capabilities: A comprehensive review," *Frontiers in Robotics and AI*, vol. 8, 2022.
- [39] E. Aucone, S. Kirchgeorg, A. Valentini, L. Pellissier, K. Deiner, and S. Mintchev, "Drone-assisted collection of environmental dna from tree branches for biodiversity monitoring," *Science Robotics*, vol. 8, no. 74, 2023.
- [40] A. Firouzeh, J. Lee, H. Yang, D. Lee, and K.-J. Cho, "Perching and grasping using a passive dynamic bioinspired gripper," *IEEE Transactions on Robotics*, vol. 40, pp. 213–225, 2024.
- [41] D. Mehanovic, D. Rancourt, and A. L. Desbiens, "Fast and efficient aerial climbing of vertical surfaces using fixed-wing uavs," *IEEE Robotics and Automation Letters*, vol. 4, no. 1, pp. 97–104, 2019.
- [42] W. R. T. Roderick, M. R. Cutkosky, and D. Lentink, "Bird-inspired dynamic grasping and perching in arboreal environments," *Science Robotics*, vol. 6, no. 61, 2021.
- [43] P. Spieler, S. X. Wei, M. Li, A. Galassi, K. Ueckert, A. Kalantari, and J. W. Burdick, "Parsec: An aerial platform for autonomous deployment

- of self-anchoring payloads on natural vertical surfaces,” in *2023 IEEE International Conference on Robotics and Automation (ICRA)*, 2023, pp. 5331–5337.
- [44] K. Bodie, M. Brunner, M. Pantic, S. Walser, P. Pfändler, U. Angst, R. Siegwart, and J. Nieto, “Active interaction force control for contact-based inspection with a fully actuated aerial vehicle,” *IEEE Transactions on Robotics*, vol. 37, no. 3, pp. 709–722, 2021.
- [45] J. Ham, T. M. Huh, J. Kim, J. Kim, S. Park, M. R. Cutkosky, and Z. Bao, “Porous dielectric elastomer based flexible multiaxial tactile sensor for dexterous robotic or prosthetic hands,” *Advanced Materials Technologies*, vol. 8, no. 3, 2022.
- [46] Y. Xia, H. Gu, L. Xu, X. D. Chen, and T. V. Kirk, “Extending porous silicone capacitive pressure sensor applications into athletic and physiological monitoring,” *Sensors*, vol. 21, no. 4, p. 1119, 2021.
- [47] C. Pichler, S. Oberparleiter, and R. Lackner, “Scott blair fractional-type viscoelastic behavior of thermoplastic polyurethane,” *Polymers*, vol. 15, no. 18, p. 3770, 2023.
- [48] M. R. Cutkosky and J. Ulmen, “Dynamic tactile sensing,” in *The Human Hand as an Inspiration for Robot Hand Development*. Springer International Publishing, 2014, p. 389–403.
- [49] S. O’Sullivan, R. Nagle, J. A. McEwen, and V. Casey, “Elastomer rubbers as deflection elements in pressure sensors: investigation of properties using a custom designed programmable elastomer test rig,” *Journal of Physics D: Applied Physics*, vol. 36, no. 15, p. 1910–1916, Jul. 2003.
- [50] J. C. Lötters, W. Olthuis, P. H. Veltink, and P. Bergveld, “The mechanical properties of the rubber elastic polymer polydimethylsiloxane for sensor applications,” *Journal of Micromechanics and Microengineering*, vol. 7, no. 3, p. 145–147, Sep. 1997.
- [51] A. N. Gent, “On the relation between indentation hardness and young’s modulus,” *Rubber Chemistry and Technology*, vol. 31, no. 4, pp. 896–906, 1958.
- [52] J. Haddow and R. Ogden, “Compression of bonded elastic bodies,” *Journal of the Mechanics and Physics of Solids*, vol. 36, no. 5, p. 551–579, 1988.
- [53] E. Cho, L. L. Y. Chiu, M. Lee, D. Naila, S. Sadanand, S. D. Waldman, and D. Sussman, “Characterization of mechanical and dielectric properties of silicone rubber,” *Polymers*, vol. 13, no. 11, p. 1831, Jun. 2021.
- [54] S. R. Williams, J. M. Suchoski, Z. Chua, and A. M. Okamura, “A 4-degree-of-freedom parallel origami haptic device for normal, shear, and torsion feedback,” *IEEE Robotics and Automation Letters*, vol. 7, no. 2, pp. 3310–3317, 2022.
- [55] T.-Y. Fang, H. K. Zhang, R. Finocchi, R. H. Taylor, and E. M. Boctor, “Force-assisted ultrasound imaging system through dual force sensing and admittance robot control,” *International journal of computer assisted radiology and surgery*, vol. 12, pp. 983–991, 2017.
- [56] A. Chiradejnant, J. Latimer, and C. G. Maher, “Forces applied during manual therapy to patients with low back pain,” *Journal of manipulative and physiological therapeutics*, vol. 25, no. 6, pp. 362–369, 2002.
- [57] W. Xie and N. Correll, “Towards forceful robotic foundation models: a literature survey,” 2025.
- [58] A. A. Hulaibi, H. Wahid, S. A. Saif, J. Sadeq, S. Esmaceli, and M. Kandil, “Skybot - a novel autonomous window cleaning drone,” in *International Conference on Electrical, Communication and Computer Engineering*, 2023, pp. 1–6.
- [59] D. Mellinger and V. Kumar, “Minimum snap trajectory generation and control for quadrotors,” in *2011 IEEE international conference on robotics and automation*. IEEE, 2011, pp. 2520–2525.
- [60] K. Watanabe, M. Aoi, M. Komatsu, S. Tanaka, and M. Nagata, “Measurements of electromagnetic emission nearby a compact drone,” in *Asia-Pacific International Symposium on Electromagnetic Compatibility*. IEEE, 2021, pp. 1–4.
- [61] M. R. Cutkosky and W. Provancher, “Force and tactile sensing,” in *Springer Handbook of Robotics*. Springer International Publishing, 2016, p. 717–736.
- [62] Z. Chua and A. M. Okamura, “A modular 3-degrees-of-freedom force sensor for robot-assisted minimally invasive surgery research,” *Sensors*, vol. 23, no. 11, p. 5230, May 2023.
- [63] J. Janeiro-Arocas, J. Tarrío-Saavedra, J. López-Beceiro, S. Naya, A. López-Canosa, N. Heredia-García, and R. Artiaga, “Creep analysis of silicone for podiatry applications,” *Journal of the Mechanical Behavior of Biomedical Materials*, vol. 63, pp. 456–469, 2016.
- [64] L. Wang, F. Ma, Q. Shi, H. Liu, and X. Wang, “Study on compressive resistance creep and recovery of flexible pressure sensitive material based on carbon black filled silicone rubber composite,” *Sensors and Actuators A: Physical*, vol. 164, no. 2, pp. 207–215, 2011.